國 立 交 通 大 學

材 料 科 學 與 工 程 研 究 所

碩 士 論 文

碳含量對鐵-8.8 鋁-30 錳-4 鉻-碳合金顯微結構與孔蝕之影響

Effects of Carbon Content on Pitting Corrosion and As-quenched Microstructure in Fe-8.8Al-30Mn-4Cr-C Alloy

研 究 生：郭 柏 村

指導教授：劉 增 豐 博士

中 華 民 國 九 十 五 年 六 月

碳含量對鐵-8.8 鋁-30 錳-4 鉻-碳合金顯微結構與孔蝕之影響

Effects of Carbon Content on Pitting Corrosion and As-quenched Microstructure in Fe-8.8Al-30Mn-4Cr-C Alloy

研 究 生：郭 柏 村　　Student：Po-Tsun Kuo

指導教授：劉 增 豐 博士　Advisor：Dr. Tzeng-Feng Liu

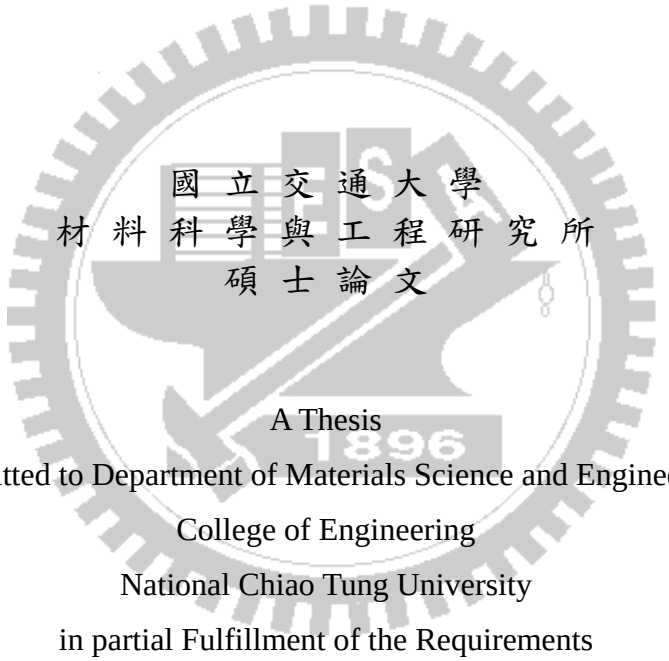

國 立 交 通 大 學

材 料 科 學 與 工 程 研 究 所

碩 士 論 文

A Thesis

Submitted to Department of Materials Science and Engineering

College of Engineering

National Chiao Tung University

in partial Fulfillment of the Requirements

for the Degree of

Master

in

Materials Science and Engineering

June 2006

Hsinchu, Taiwan, Republic of China

中 華 民 國 九 十 五 年 六 月

誌 謝

由衷地感謝指導教授劉增豐博士兩年來的悉心指導與諄諄教誨，使得學生在研究過程中得以順利進行，並如期完成本論文。在此特別對吾師劉增豐教授以及師母林美慧老師致上最大的敬意與誠摯的謝意。

在這段研究期間，承蒙學長李堅瑋博士的提攜，使學生在論文實驗方向及解決問題上獲得該具備的研究方式與態度，加上論文寫作上的指導與協助，實讓學生獲益匪淺。另外，更應該感謝各位博士班的學長王承舜、楊勝裕、段逸軒、蘇俊偉以及林志龍學長，由於他們在各項儀器操作分析以及生活上諸多事項的給予指導，使我能夠在研究經驗上很快地步上軌道。同時也獲得同學陳信良、蔡明諺以及學弟蔡雨霖、陳柏至和王浩仰，在實驗上的協助及精神上的支持，幫我節省了許多寶貴的時間，由衷感激。一路走來受到實驗室學長學弟一貫的相互扶持與鼓勵使得我在研究過程中倍感溫馨，尤其國科會在研究經費上之贊助，使得本論文得以順利完成，在此一併致上衷心的謝意。

最後，僅將本論文獻給我最辛苦的父母，以及我最疼愛的弟弟，感恩有他們多年來的悉心照顧與無限的關心，使我能在安心的環境下順利完成學業。

摘 要

本實驗利用極化及浸泡測試來研究碳含量在 0.06 到 1.58 wt.%的鐵-8.8鋁-30錳-4鉻-碳合金，於淬火狀態下對孔蝕行為的影響。經由TEM、SEM、EDS和AES的分析，可以將此不同碳含量的合金分為三種，分別為麻田散鐵型、(α+γ) 雙相型和沃斯田鐵型(γ) 鐵鋁錳鉻碳合金。

在麻田散鐵型合金中，由於 18R 麻田散鐵的形成導致應力場產生，因此孔蝕容易發生在麻田散鐵和肥粒鐵基材之間。隨著碳含量由 0.06 增加到 0.61 wt.%，沃斯田鐵相逐漸增加，但是由於 18R 麻田散鐵仍存在於肥粒鐵基地中，因此孔蝕電位無法大幅地提升。此外，當 18R 麻田散鐵在肥粒鐵基地中消失時，很明顯地可以增加抗孔蝕的能力，而且發生孔蝕的地方則由 α / γ 晶粒邊界取而代之。接著增加碳含量會造成沃斯田鐵基地中有細微的 κ' 相產生，由於此 κ' 相與基地間具有較低的介面能，所以對於孔蝕並沒有太大的影響。然而殘留的硫化錳和氧化鋁的夾渣物，對於具抗孔蝕佳的沃斯田鐵相有較大的傷害影響。

Abstract

The pitting corrosion behaviors of the as-quenched Fe-8.8Al-30Mn -4Cr-C alloys with various carbon contents in the range from 0.06 to 1.58 wt.% were studied by potentiodynamic polarization and immersion tests. Through TEM, SEM, EDS and AES analyses, the alloys examined can be classified into three main groups, namely martensitic, (α+γ) duplex and austenitic(γ) alloys.

In martensitic alloys, great strain-field accompanying by the formation of the 18R martensite results in favorable sites for the pitting nucleation between the martensite and the ferrite matrix. The volume fraction of the austenite phase was increased with increasing the carbon content ranging from 0.06 to 0.61 wt%. However, there was no obvious rise in the critical pitting potential while the 18R martensite was still present. Besides, the pitting resistance of the duplex alloy could be noticeably improved as a result of the absence of the 18R martensite. In the meanwhile, the α/γ grain boundaries substituted the initial pitting sites for the 18R martensite in the duplex alloys. When the carbon content was high enough to form the fine κ'-carbides within the austenite matrix, the lower coherent interfacial and strain energies would have no detrimental

effect on the pitting corrosion resistance. The retained inclusions of manganese sulfide and aluminum oxide, however, were responsible for the deterioration in the pitting resistance of the austenite phase.

Contents

List of Figures

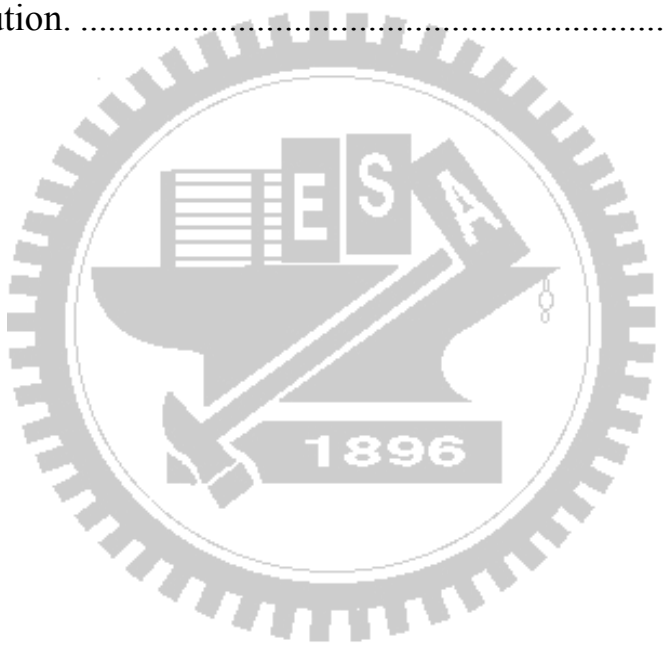

List of Tables

Introduction

The Fe-Al-Mn alloys, substituting manganese and aluminum for the strategic and expensive alloying elements of nickel and chromium contained in the conventional Fe-Ni-Cr-based stainless steels, have attracted much attention due to the relatively low cost of raw materials and the abundant reserves of both manganese and aluminum in the earth [1-4]. Unfortunately, although the Fe-Al-Mn alloys have a higher corrosion resistance than carbon steels, they are still far inferior to that of the conventional stainless steels [5-18]. Later, a considerable amount of interest has been focused on developing carbon-contained Fe-Al-Mn-C alloys as high strength and ductility alloy steels, which have a lower density than the carbon steels or the stainless steels by 15~20 percent because of the addition of 6~10 wt.% aluminum [19-33].

Although the Fe-Al-Mn-C alloys possess the excellent mechanical and physical properties, the relatively lower corrosion resistance restricts their extensive applications in industry. Consequently, approaches were made to further improve the corrosion resistances of the Fe-Al-Mn-C alloys by either the surface treatments or the chemical compositional

modifications. Surface treatments such as electroplating, pack chromizing, aluminization, physical vapor deposition, etc., were reported to be capable of raising the corrosion resistances of the Fe-Al-Mn-C alloys [33-35].

It is also confirmed that the addition of a small amount of chromium or the combination of silicon or molybdenum can effectively improve the corrosion resistances of the Fe-Al-Mn-C alloys [36-38]. After the modifications of the chemical compositions, it is available for the Fe Al-Mn-Cr-C alloys to be applied to mildly corrosive working environments. In recent years, some commercial products requiring the characteristics of light weight, high strength and excellent ductility, such as sporting goods of golf club heads, vehicle parts, etc., were made from Fe-Al-Mn-Cr-C alloys and have already been commercialized.

For the Fe-Al-Mn-based alloys, the pitting attack is the primary corrosion behavior rather than the general corrosion [8-17]. It is known that the pitting corrosion is strongly related to the microstructural factor. The variation in carbon content has an important influence on the microstructural change in the Fe-Al-Mn-based alloys. So far, most investigations on the corrosion of the Fe-Al-Mn-based alloys were

focused on the electrochemical corrosion measurements [15-17,36-38]. However, the information concerning the effect of the microstructural change on the pitting corrosion behaviors is very deficient. Therefore, the aim of this study is to determine the relationship between the as-quenched microstructure and the susceptibility to the localized pitting corrosion in the Fe-8.8Al-30Mn-4Cr-C alloys with various carbon content by means of transmission and scanning electron microscopy.

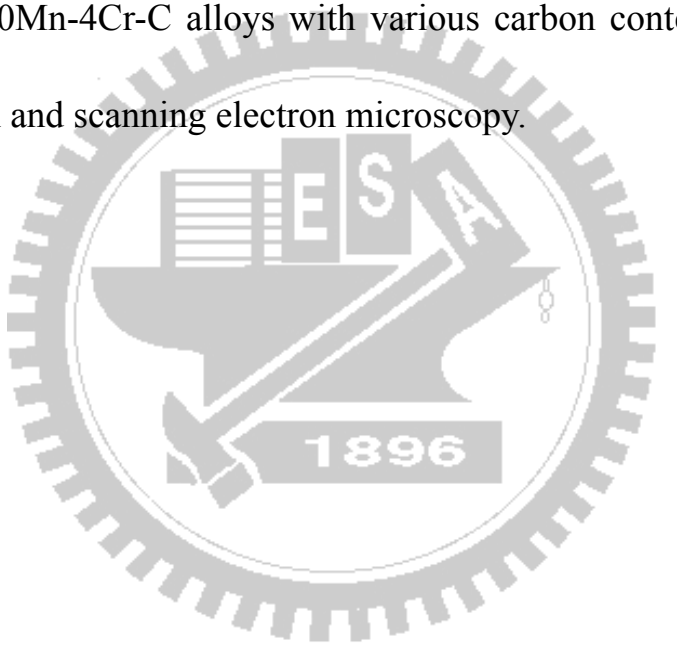

Experimental procedure

(A) Alloy preparation

Seven Fe-8.8Al-30Mn-4Cr-(0.06~1.58)C alloys examined in the present study were prepared in an air induction furnace by using 99.9 pct iron, 99.7 pct aluminum, 99.9 pct electrolytic manganese, 99.6 pct chromium, 99.5 pct nickel and pure carbon powder. The melt was chill cast into 30×50×200 mm-iron mold. After being homogenized at 1150 ℃ for 72 hours, the igots were sectioned into 2-mm-thick silices. These silices were subsequently solution heat-treated at 1150 ℃ for 3 hours followed by a rapid quench into iced water. The chemical compositions of the present alloys were analyzed by inductively coupled plasma-mass spectrometer (ICP). The results are shown in Table I.

(B) Electrochemical potentiodynamic polarization test

Potentiodnamic polarization curves were measured in aerated 3.5 % Sodium Chloride (NaCl) solution at room temperature. Electrochemical polarization curves were obtained by using an EG&G Princeton Applied Research Model 273 galvanostat/potentiostat, a computer, amd recorder and were corrected for ohmic effect. A conventional three-electrode cell

was used, and all potentials were reported with respected to a saturated calomel electrode (SCE). Electrochemical tests were carried out in a glass cell filled with ~ 300ml of test solution maintained at 25 ± 2 ℃. Samples with an exposed surface area of ~ 1 cm^2 were wet polished using silicon carbide (SiC) paper to 1,500 grit,washed in distilled water, and rinsed in acetone prior to polarization. The specimens were immersed in the solutions for about 30 min until a stable corrosion potential (E_{corr}) was obtained, and then the polization was initiated at 500 mV negative to, followed by scanning toward noble direction at a rate of 0.5 mV/s.

(C) Microstructure observation and diffaction analysis

(1) Transmission electron microscopy (TEM)

The transmission electron microscopy specimens were prepared by means of a double jet electropolisher with an electrolyte of 15 % perchloric acid, 25 % acetic acid and 60 % ethanol. The polishing temperature was kept in the range from -30 ℃ to -20 ℃ and the current density was kept in the range from 3.5 to 4×10^4 A/m^2. Electron microscopy was performed on a JEOL-2000FX scanning transmission electron microscope (STEM) operating at 200 kV.

(2) Scanning electron microscopy (SEM)

The samples of scanning electron microscopy were obtained similar to STEM samples. Scanning electron microscopy was performed on a JEOL-6500FX Field-emission SEM operating at 15 kV. The SEM microscopy was equipped with an energy-dispersive X-ray spectrometer (EDS) for chemical analysis and distribution. Quatitative analysis of elemental concentrations for Fe, Al, Mn and Cr were with the aid of a Cliff-Lorimer ration Thin Section method.

(D) Immersion test

The immersion test was carried out in 6 wt% Ferric Chlorde ($FeCl_3$) solution. Specimens, 9 mm × 9 mm × 1.3 mm, were tested. The surfaces of the samples were polished with SiC paper to 1,200 grit. The Specimen contained in the cradle was placed inside a 300ml beaker and completely immersed in the test solution. Once taken out of the solution, the specimens were not used for the next immersion. The surfaces of the speciments were examined systematically by scanning electron microscopy.

(E) Auger electron spectroscopy (AES) examination

Specimens for the Auger electron spectroscopy examination were held at a constant passive potential corresponding to the passive region of

the alloys for 20 min in the sodium chloride solution, and the compositions of the elements in the passive film were examined. The energy of the primary electron beam and the Ar^+ sputtering beam is 3 and 2.5 keV, respectively. The Auger peaks recorded were Fe (648 eV), Mn (587 eV), Al (1394 eV), O (506 eV), Cr (489 eV), Ni (846 eV) and C (266 eV).

Results and discussion

A. Effect of the carbon content on the potentiodynamic polarization curve

In this study, the potentiodynamic polarization test was first employed to assess the pitting corrosion resistance of seven Fe-Al-Mn -Cr-C alloys containing carbon content in the range from 0.06 to 1.58 wt.% in a 3.5 wt.% sodium chloride (NaCl) solution at room temperature. The critical pitting potentials (E_{pp}) were measured as the potential at which there was a drastic rise in the current density with further scanning potential up. The sharp increase is due to the severe localized attack. Thus, the critical pitting potential is thought to be indicative of the susceptibility to the pitting corrosion, that is, a higher critical pitting potential implies a higher pitting corrosion resistance. Figure 1 shows the polarization curves of these seven alloys. The results of critical pitting potential and current density determined from each polarization curve are listed in Table Ⅱ for comparison. It is apparent that there is a general tendency to a higher critical pitting potential with a higher carbon content. From the experimental results, the variations in the critical pitting potentials of the alloys are worthy to note. For the alloys with carbon content in the range

from 0.06 to 0.61 wt.%, there is a slight increase in the critical pitting potential with increasing the carbon content. However, both the relatively obvious rises can be observed with increasing the carbon content from 0.61 to 0.72 and 0.72 to 0.93 wt.%. Subsequently, when the alloys contain higher carbon content from 0.93 to 1.58 wt.%, the critical pitting potentials are still kept. Therefore, it can be concluded from the potentiodynamic polarization test that the pitting resistance of the Fe-Al-Mn -Cr-C alloy can be effectively improved until up to 0.93 wt.% carbon content, but it does not increase any more with further increasing from 0.93 to 1.58 wt.%.

B. TEM and SEM investigations on the as-quenched microstructures

It is well known that metallurgical character is one of the most important factors to affect the susceptibility to the pitting corrosion, so that it is essential to evaluate the as-quenched microstructures of the alloys with various carbon content. Figure 2(a) is a scanning electron micrograph of the as-quenched alloy A, exhibiting ferrite grains. Figure 2(b), a higher magnification micrograph, clearly reveals the presence of needle-like phase with specific orientations within the ferrite matrix. In order to identify the needle-like phase, transmission electron microscopy examinations of thin foils were performed. Figures 2(c) through (e) are a bright-field electron micrograph and two selected-area patterns taken from a needle-like phase and its surrounding ferrite matrix. Compared to the previous studies [39-55], it is clear that the needle-like phase is 18R martensite.

Figure 3(a) is a scanning electron micrograph of the as-quenched alloy B. Since carbon is a strong austenite-stabilizing element, the austenite(γ) grains with annealing twins started to appear. No precipitates could be detected within the austenite grains by either scanning or transmission electron microscopy, however, a high density of the

needle-like 18R martensite can still be found within the ferrite(α) grains, as shown in Figure 3(b). It is worthy to note in Figure 3(b) that wide and rather narrow martensite-free zones (MFZs) inside the ferrite grains can be seen along the α/γ and α/α grain boundaries, respectively. It was proposed that the MFZs were distributed to the lack of critical nucleation of vacancy [40-41]. But this can not explain the discrepancy in MFZs between along the α/γ and α/α grain boundaries. The fact that no needle-like 18R martensite was found in the carbon-free Fe-7.5Al -30Mn alloy [44], indicating that the carbon may play an important role in the formation of the 18R martensite. Thus, in addition to the effect of vacancy concentration, the MFZs are thought to be due to the depletion of the carbon atoms which diffused to the nearby austenite phases. Owing to a higher carbon solubility in comparison with the ferrite phase [43], therefore, the width along the α/γ grain boundary was large than that along α/α grain boundary. Otherwise, the width of the MFZs should be similar regardless of kinds of grain boundaries.

Along with increasing the carbon content to 0.61 wt.%, in addition to the increase in the volume fraction of the austenite phase, there is no difference in the microstructural constitution between the alloy B and

alloy C, as shown in Figures 4 (a) and (b). The needle-like 18R martensite and the MFZs could still be found in the alloy C. Consequently, the microstructure of the alloy C in the as-quenched condition consists of a mixture of austenite, ferrite and 18R martensite.

Similarly, the volume fraction of the austenite phase continued to increase with increasing the carbon content to 0.72 wt.%. In the alloy D, the austenite phase becomes predominant and some relatively small and discrete ferrite grains are present along the austenite grain boundaries, as shown in Figure 5. No precipitates could be detected within the austenite grains by means of the transmission electron microscopy. In contrast to the alloys with 0.06, 0.32 and 0.61 wt.% carbon, the formation of the 18R martensite within the discrete ferrite grains in the alloy D is absent. As a result, the microstructure of the as-quenched alloy D is composed of the duplex phases of austenite and ferrite.

Figure 6 is a scanning electron micrograph of the alloy E in the as-quenched condition, exhibiting a single-phase austenite with annealing twins. This indicates that the addition of 0.93 wt.% carbon is high enough to stabilize the full austenite phase in the Fe-8.8Al-30Mn-4Cr alloy at the solution heat treating temperature. Also, no precipitates could be detected

within the austenite phase by either SEM or TEM.

Figure 7(a) shows a scanning electron micrograph of the as-quenched alloy F. The morphology shown in Figure 7(a) may suggest that the microstructure is still a single-phase austenite. However, the bright-field electron micrograph reveals that a high density of fine precipitates with a modulation structure was formed within the austenite matrix, as shown in Figure 7(b). Figure 7(c), a selected-area diffraction pattern taken from a mixed region covering the austenite matrix and fine precipitates, indicates that the fine precipitates are $(Fe,Mn)_3AlC_x$ cabides (designated as κ'-carbides) having an $L'1_2$-type structure [56-66]. In Figure 7(c), it is also seen that satellites lying along <001> reciprocal lattice directions about the (200) and (220) reflections can be observed. The existence of the satellites demonstrates that the fine κ'-carbides were formed during quenching by a spinodal decomposition. Figure 7(d) is a (010) κ'-carbides dark-field electron micrograph of the as-quenched alloy F, clearly showing the presence of the extremely fine κ'-carbides. Accordingly, the as-quenched microstructure of the alloy F is austenite phase containing extremely fine κ'-carbides. Transmission electron microscopy of thin foils indicated that the as-quenched microstructure of the alloy G with 1.58

carbon content is similar to that of the alloy F.

C. SEM observations on the pitting corrosion behaviors

In order to investigate the susceptible areas and the modes of pitting attack, the present specimens after the immersion test in 6 wt.% ferric chloride solution were subjected to the scanning electron microscopy observation. Moreover, the fresh specimens were held at potentials just slightly above their critical pitting potentials in a 3.5 wt.% sodium chloride (NaCl) solution at room temperature to accelerate the pitting corrosion and then examined by the scanning electron microscopy to observe the behavior of the pit propagation. In Figure 8(a), it can be seen that the localized attacks are clearly found to be around the 18R martensite in the initial stage of the pitting corrosion after the alloy A was immersed in ferric chloride for a short time period. With raising immersing time, there are a large number of growing pits in the interiors of the ferrite grains but along the α/α grain boundaries, as shown in Figure 8(b). This indicates that the 18R martensite is much more susceptible to the pitting attack than the α/α grain boundary. Figure 8(c) exhibits a severely corroded surface after applying a pitting potential to the alloy A, revealing that the pitting attacked areas extended to the α/α grain boundaries and the whole ferrite grains.

For the alloy B, the 18R martensite interfaces also act as the nucleation sites for the pitting corrosion in the immersion test and the subsequent attack, which caused pits to coarsen and grow inside the ferrite grains. The examples are shown in Figures 9(a) and (b). It can be seen in the Figure 9(a) that the absence of the pits can be observed in the vicinity of the α/γ grain boundaries where MFZs are present. In addition, there are only a few pits inside the austenite grains in comparison with the ferrite grains. Based on the energy-dispersive spectrometer (EDS) analysis, it is verified that such pits occurred inside the austenite grains are attributed to two kinds of inclusions. One is the manganese sulfide and the other is the aluminum oxide, which were produced during the melting process and retained in the ingot as solidifying. Figure 9(c) shows that the whole ferrite grains were severely corroded after applying a pitting potential to the alloy B. From these observations through Figures 9(a) to (c), it is suggested that the pits initiated at the 18R martensite interfaces in the interiors of the ferrite grains and then gradually grew towards the grain boundaries. Eventually, the pitting attack occupied the whole ferrite grains. However, on the other hand, in addition to a few pits due to the existence of the manganese sulfide and aluminum oxide

inclusions, no other pits related to the microstructural factors could be found inside the austenite grains.

The similar mode of the pitting corrosion was also found to occur in the alloy C. Compared to the alloy B, the severely pitting attacked area is reduced with the increase in the volume fraction of the austenite phase in the alloy C, as shown in Figure 10. However, for the alloy D, there is a reverse sequence of the pitting attack in the ferrite grains in comparison with the Fe-8.8Al-30Mn-4Cr alloys containing 0.06, 0.32 and 0.61 wt.% carbon. As can be seen in Figures 11(a) and (b), the nucleation of the pits occurred first at the α/γ grain boundaries rather than inside the ferrite grains. Subsequently, the pitting attacks proceeded to the interior of the relatively small and discrete ferrite grains. Although the mode of the pitting attack inside the ferrite grains is quite different as increasing carbon content from 0.61 to 0.72 wt%, the existence of the inclusions is still the main reason to facilitate the pitting corrosion in the austenite grains.

For the alloy E having an as-quenched microstructure of a single-phase austenite, neither grain nor twin boundaries are found to be the initiation sites of the pitting corrosion. As can be seen in Figure 12(a),

the pitting corrosion originating from the inclusions becomes predominant in the single-phase austenite, where the pits were dispersed at random within the austenite matrix. It is seen in Figure 12(b) that the larger and deeper pits followed the inclusion-induced pits after applying a pitting potential to the alloy E.

From the microstructural observations mentioned above, as increasing the carbon content to 1.25 or 1.58 wt.%, the formation of the fine κ'-carbides within the austenite matrix is present. It is interesting to know whether the existence of the fine κ'-carbides will deteriorate the pitting resistance of the austenite phase or not. Figures 13(a) and (b) are two scanning electron micrographs after the immersion and accelerated pitting corrosion tests, respectively. Compared to the alloy E, there appears to be no difference in the behavior of the pitting attack between the austenite matrix with and without the precipitation of the fine κ'-carbides. The existence of the retained inclusions is believed to be the reason to cause the pitting corrosion in the austenite grains. There are no evidences that the pitting attack is related to the precipitation of the fine κ'-carbides.

D. Relationship between the pitting corrosion behaviors and the microstructures

On the basis of the above observations, the pitting corrosion behaviors of the as-quenched alloys with various carbon contents are strongly related to their microstructures. Some discussion in detail will be given below. The present Fe-8.8Al-30Mn-4Cr alloys containing from 0.06 to 1.58 wt.% carbon can be classified into the three main groups, namely the martensitic, (α+γ) duplex and austenitic alloys, depending on not only the as-quenched microstructural differences and the resistances of the pitting corrosion. The martensitic alloys contain carbon contents in the range of 0.06 to 0.61 wt.%. They are called martensitic alloys since the 18R martensite formed within the ferrite phase during quenching. In these martensitic alloys, great strain-field accompanying by the formation of the 18R martensite is developed around the martensite, so that the interfaces between the martensite and the ferrite matrix provide much favorable sites for the pitting nucleation. The 18R martensite interfaces were observed to be attacked by the pitting corrosion in preference to not only the α/α but also the α/γ grain boundaries. It is thus to suggest that the 18R martensite is the most sensitive to the pitting corrosion due to the

great strain-field around them. The absence of the pits in the vicinity of the α/γ grain boundaries in the martensitic alloys can be formed as a result of the wide MFZs along the α/γ grain boundaries. This leads to the pitting attack from the interiors of the ferrite grains to their grain boundaries in sequence. The martensitic alloys can be further subdivided into both with and without austenite phase. The volume fraction of the austenite phase is increased with increasing the carbon content ranging from 0.06 to 0.61 wt.%. Since the ferrite grains contain a high density of the 18R martensite, the pitting corrosion resistance should be increased along with increasing the volume fraction of the austenite and vice versa. However, no obvious rise in the critical pitting potential is expected while the 18R martensite is still present. Therefore, it is appropriate to propose that the martensitic alloy A without the austenite phase has the worst resistance to the pitting corrosion. When the carbon content increased from 0.06 to 0.61 wt.%, the pitting corrosion resistance of the martensitic alloys can slightly be improved. This is in agreement with the results obtained from the potentiodynamic polarization test in Figure 1.

The present alloy containing 0.72 wt.% carbon belongs to one of the duplex (α+γ) alloys. They are called duplex since their microstructures

essentially consist of duplex phase of austenite and ferrite in the as-quenched condition. The absence of the 18R martensite distinguishes the duplex from martensitic alloys. Because the volume fraction of the ferrite phase is further reduced with increasing the carbon content in the alloy, the ferrite grains gradually change to smaller and discrete ones. Based on the reason for the formation of the MFZs mentioned above, once the ferrite grains are small enough and/or the MFZs are wide enough to lead to a depletion of carbon in the interiors of the ferrite grains, the martensite-free ferrite grains will be resulted. It is reasonable to believe that the pitting resistance of the duplex alloys can be noticeably improved as a result of the absence of the 18R martensite, which is the most susceptible to the pitting attack. The obvious rise in the critical pitting potential of the duplex alloy D is reflective of such a change in the microstructure. Additionally, the α/γ grain boundaries as the substitutes for the 18R martensite to be the initiation sites for the pitting attack can be observed in the duplex alloys, since they are energetically favorable nucleation sites in comparison with the γ/γ grain boundaries or twin boundaries. From the experimental results, the pitting initiation at the α/γ grain boundaries was followed by a sequence of the pitting attack inside

the ferrite grains rather than the austenite grains. This implies that the ferrite phase is more susceptible to the pitting corrosion than the austenite phase in the Fe-8.8Al-30Mn-4Cr alloys. In order to obtain more information, concentration depth profiles for elements from the surface on the passivated duplex alloy D held at a constant passive potential for 20 minutes were examined by using the auger electron spectroscopy (AES). The profiles of atomic concentrations against sputtering time taken from the austenite and ferrite phases were illustrated in Figures 14(a) and (b), respectively. The decrease in oxygen concentration indicates that the metallic elements were transferred from the oxidative to metallic state, and the region detected by AES was approached to alloy substrate while the passive film was successively removed with increasing sputtering time. The detection of high concentration of carbon was due to the existence of contamination on the surface. In Figures 14(a) and (b), the concentrations of the aluminum and chromium in the passive film are much greater than that in the alloy substrate, and the reverse result is obtained for the concentrations of the iron and manganese. The contributions of the aluminum and chromium in the passive film are referred to the presence of the protective aluminum and chromium oxide

scales. The thickness of the oxide layer was determined as the depth at which the oxygen concentration dropped to half of the highest value [15]. Comparing Figure 14(a) with (b), it is clearly seen that the passive film on the austenite phase is much thicker than that on the ferrite phase. This is the reason why the austenite phase possesses a superior pitting corrosion resistance to the ferrite phase. But further investigation is required to know why the austenite phase has a thicker passive film than the ferrite phase in the duplex alloys.

The present alloys containing carbon contents ranging from 0.72 to 1.58 wt.% belong to the group of the austenitic alloys. They are called austenitic since their microstructures essentially comprise a single-phase austenite. In consequence of the absence of the ferrite phase and the α/γ grain boundaries with a higher energy than the γ/γ grain boundaries, the pitting corrosion resistance or the critical pitting potential can be further significantly increased, corresponding to the results shown in Figure 1. The austenitic alloys can be further subdivided into both with and without the κ'-carbides. By the formation of the fine κ'-carbides, the strength of the austenitic alloy can be greatly increased without significant loss in ductility. The existence of the fine κ'-carbides is thought to be beneficial

to the mechanical properties of the austenitic alloys. On the other hand, the effect of the fine κ'-carbides on the pitting corrosion is evaluated in the present study. Based on the above experimental results for the alloy E and alloy F, similar behaviors of the pitting attack could be observed regardless of the existence of the fine κ'-carbides. From the transmission electron microscopy analysis, the fine κ'-carbides having an ordered FCC structure of $L'1_2$-type were formed within the austenite phase with a disordered FCC structure during quenching by spinodal decomposition, so that the rather low values of the coherent interfacial and strain energies between the fine κ'-carbide and the austenite matrix would be resulted. It is thus to suggest that there is no detrimental effect of the existence of the fine κ'-carbides on the pitting corrosion resistance. This is consistent with the results obtained from the potentiodynamic polarization test.

Finally, the inclusions of manganese sulfide and aluminum oxide are frequently found in the alloys since the manganese has a strong affinity to sulfur and the aluminum can be oxidized with much ease at melting temperature about 1600℃. From the above examinations, the retained inclusions are responsible for the deterioration in the pitting resistance of the austenite phase. It is thus to believe that the pitting corrosion

resistance will be further improved if the inclusions can be avoided to retained in the Fe-Al-Mn-Cr-C alloys.

Conclusions

On the basis of the above observations, the pitting corrosion behaviors of the as-quenched Fe-8.8Al-30Mn-4Cr-C alloys with various carbon content are strongly related to their microstructures. Some conclusions will be given below.

(1) In martensitic alloys, great strain-field accompanying by the formation of the 18R martensite is developed around the martensite, so that the interfaces between the martensite and the ferrite matrix provide favorable sites for the pitting nucleation.

(2) The volume fraction of the austenite phase increased with increasing the carbon content ranging from 0.06 to 0.61 wt.%. There is no obvious rise in the critical pitting potential as the 18R martensite is still present.

(3) The pitting resistance of the duplex alloys can be noticeably improved as a result of the absence of the 18R martensite which is the most susceptible to the pitting attack.

(4) The α/γ grain boundaries as the substitutes for the 18R martensite to be the initiation sites for the pitting attack in the duplex alloys.

(5) Owing to the lower coherent interfacial and strain energies between the fine κ'-carbide and the austenite matrix, there is no detrimental effect of the existence of the fine κ'-carbides on the pitting corrosion resistance.

(6) The retained inclusions of manganese sulfide and aluminum oxide are responsible for the deterioration in the pitting resistance of the austenite phase.

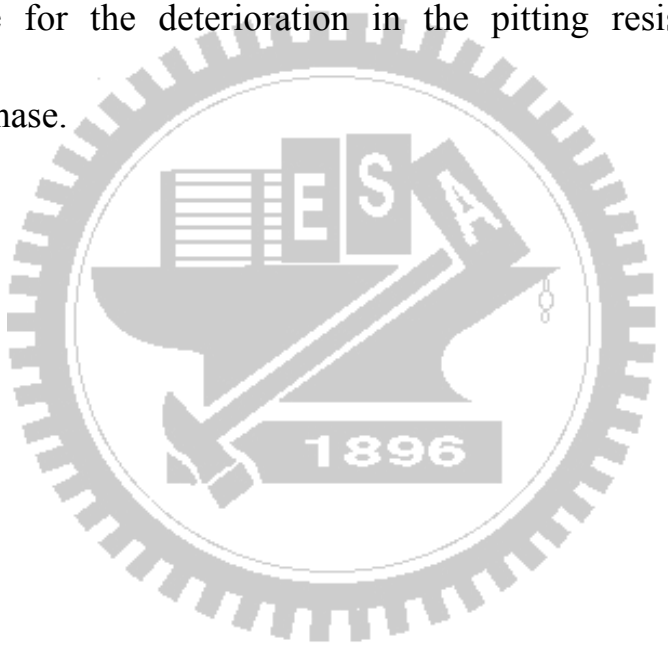

References

1. Samir K. Banerji, Metal Progress April (1978) 59.
2. R. Wang and F. H. Beck, Metal Progress March (1983) 73.
3. John S. Dunning, Max L. Glenn and Howard W. Leavenworth Jr. Metal Progress October (1984) 19.
4. J. C. Benz and H. W. Leavenworth Jr. Journal of Metals March (1985) 36.
5. S. C. Tjong, Sur. and Coat. Tech. 28 (1986) 181.
6. W. T. Tsai, J. B. Bang, J. T. Lee, J. Mater. Sci. 22 (1987) 3517.
7. Y. J. Gau, J. K. Wu, J. Mater. Sci. 11 (1992) 119.
8. S. T. Shin, C. Y. Tai, and T. P. Perng, Corrosion 49 (1993) 130.
9. S. T. Shih, I. F. Tsu and T. P Perng, Metall. Trans. A, 24(1993) 459.
10. Y. S. Zhang, X. M. Zhu and S. H. Zhong, Mater. Tech. 64 (1993) 564.
11. K. Wright, R. N. Wright and G. A. Moore, Scripta Metall. 28 (1993) 501.
12. E. Otero, A. Pardo, M. V. U. Utrilla, E. Saenz and F. J. Perez, Mater. Charac. 35 (1995) 145.
13. M. Ruscak and T. P. Perng, Corrosion Science 51 (1995) 738.
14. Y. J. Gau, J. K. Wu, Corrosion Prevention & Control (1997) 56.
15. X. M. Zhu and Y. S. Zhang, Corrosion 54 (1998) 3.
16. J. W. Lee, J. Chin. Corr. Eng. 13(4) (1999) 139.
17. Y. S. Zhang and X. M. Zhu, Corr. Sci. 41 (1999) 1817.
18. J. W. Lee, J. Chi. Corr. Eng. 13(4) (1999) 139.
19. H. H. Huang and T. H. Chuang, Mater. Sci. Eng. A292 (2000) 90.

20. A. A. Hashem and W. Riad, Mater. Charac. 47 (2001) 389.
21. C. J. Altstetter, A. P. Bentley, J. W. Fourie and A. N. Kirkbride, Mater. Sci. Eng 82 (1986) 13.
22. J. G. Duh, and C. J. Wang, J. Mater. 25 (1990) 2063.
23. J. G. Duh and S. C. Lin, J. Mater. Sci. 28 (1993) 5975.
24. C. J. Lin and M. T. Liao, J. Mater. Sci., April (1993) 6007.
25. C. Y. Chao, C. N. Hwang and T. F. Liu, Scripta. Metall. 34(1) (1993) 75.
26. D. S. Stone and K. B. Yodev, J. Mater. Res. 9 (1994) 2524.
27. Y. S. Han and S. H. Hong, Sci. Eng. A222 (1997) 76.
28. Y. Nishinno, A. Asano and T. Ogawa, Mater. Sci. Eng. 234 (1997) 271.
29. C. N. Hang and T. F. Liu, Script Metall. 36(8) (1997) 853.
30. W. K. Choo, J. H. Kim and J. C. Yoon, Acta Mater. 45 (1997) 4877.
31. K. Bouche, F Barbier and A. Coulet, Mater. Sci. Eng. A249 (1998) 167.
32. C. Y. Chao and C. H. Liu, Mater. Trans. 43(10) (2002) 2635.
33. C. J. Wang, J. W. Lee and T. H. Twu, Surf. Coat. Tech. 163 (2003) 37.
34. Y. S. Zhang, X. M. Zhu, M. Liu and R. X. Che, Appl. Sur. Sci. 222 (2004) 89.
35. V. F.C. Lins, M. A. Freitas and E. M. Paula e Silva, Appl. Sur. Sci. 250 (2005) 124.
36. Y. S. Zhang, X. M. Zhu and S. H. Zhong, Corr. Sci. 46 (2004) 853.
37. E. Angelini, B. D. Benedetti and F. Rosalbino, Corr. Sci. 46 (2004) 1351.
38. Y. F. Cheng, and F. R. Steward, Corr. Sci. 46 (2004) 2405.

39. S. K. Chen, W. B Lee, K. W. Chour, C. M. Wan and J. G. Byrne, Scrip. Metall. 23 (1989) 1919.
40. S. K. Chen, K. H. Hwaug, C. M. Wan and J. G. Byrne, Scrip. Metall. et Mater. 24 (1990) 151.
41. K. H. Hwang, C. M. Wan and J. G. Byrne, Scip. Metall. et Mater. 24 (1990) 979.
42. S. K. Chen, C. M. Wan and J. G. Byrne, Mat. Res. Bull. 25 (1990) 1311.
43. W. S. Yang, T. B. Wu and C. M. Wan, Scrip. Metall. et Mater. 24 (1990) 895.
44. W. S. Yang, K. H. Hwang, T. B. Wu, J. G. Byrne and C. M. Wan, Script Metall. et Mater. 24 (1990) 1221.
45. K. H. Hwang, S. K. Chen, W. S. Yang, T. B. Wu, C. M. Wan and J. G. Byrne, Scrip. Metall. et Mater. 24 (1990) 495.
46. K. H. Hwang, W. S. Yang, T. B. Wu, C. M. Wan and J. G. Byrne, Metall. Trans. A 21 (1990) 2815.
47. K. H. Hwang, W. S. Yang, T. B. Wu, C. M. Wan and J. G. Byrne, Acta metal. Mater. 39(5) (1991) 825.
48. K. H. Hwang, C. M. Wan and J. G. Byrne, Mater. Sci. Eng. A132 (1991) 161.
49. C. H. Chao and N. J. Ho, Scrip. Metall. et Mater. 26 (1992) 1863.
50. C. H. Chao and N. J. Ho, Scrip. Metall. et Mater. 27 (1992) 493.
51. C. H. Chao and N. J. Ho, Scrip. Metall. et Mater. 27 (1992) 499.
52. W. B. Lee, F. R. Chen, S. K. Chen and C. M. Wan, Scrip. Metall. et Mater. 31 (1994) 695.
53. H, Y. Chu, F. R. Chen and T. B. Wu, Scrip. Metall. et Mater. 33 (1995)

1269.

54. W. B. Lee, F. R. Chen, S. K. Chen, G. B. Olson and C. M. Wan, Acta Metall. Mater. 43 (1995) 21.
55. H, Y. Chu, F. R. Chen and T. B. Wu, Mater. Let. 30 (1997) 369.
56. D. J. Schmatz: Trans. ASM 52 (1960) 898.
57. R. E. Cairns, Jr. and J. L. Ham: U. S. Patent, (1963) No. 3111405.
58. M. F. Alekseyenko, G. S. Krivonogov, L. G. Kozyreva, I. M. Kachanova and L. V. Arapova: Met. Sci. Heat Treat. 14 (1972) 187.
59. L. I. Lysak, M. F. Alekseyenko, A. G. Drachinskaya, N. A. Storchak and G. S. Krivonogov: Metallofizika, 59 (4) (1975) 29.
60. S. K. Banerji: Met. Prog. (1978) 59.
61. J. C. Grcia, N. Rosas and R. J. Rioja: Met. Prog. (1982) 47.
62. R. Wang and F. H. Beck: Met. Prog. (1983) 72.
63. I. Briggs, G. J. Russell and A. G. Clegg: J. Mater. Sci. 20 (1985) 668.
64. K. H. Han, J. C. Yoon and W. K. Choo: Scripta Metall. 20 (1986) 33.
65. W. K. Choo and D. G. Kim: Metall. Trans. A, 18A (1987) 759.
66. S. C. Tjong and N. G, Ho: Metallography 21 (1988) 199.

Acknowledgements

The authors gratefully acknowledge the financial support for this research by the National Science Council of the Republic of China under contract no. NSC 94-2216-E-009-010.

Table Ⅰ. Chemical compositions of the Fe-8.8Al-30Mn-4Cr-C alloys examined (wt.%)

Alloy	Mn	Al	Cr	C	Fe
A	30.4	8.63	3.51	0.06	Bal.
B	29.9	8.57	3.58	0.32	Bal.
C	29.5	8.61	3.54	0.61	Bal.
D	29.7	8.58	3.59	0.72	Bal.
E	28.4	8.50	3.50	0.93	Bal.
F	30.8	8.55	3.56	1.43	Bal.
G	30.3	8.56	3.52	1.58	Bal.

Table Ⅱ. The electrochemical parameters obtained from polarization test in 3.5 % NaCl solution

Alloy	E_{corr} (mV_{sce})	E_{pp} (mVsce)	I_{corr} (A/cm^2)	I_{pp} (A/cm^2)
A	-312	-271	1.55×10^{-6}	4.98×10^{-6}
B	-301	-267	8.28×10^{-7}	3.97×10^{-6}
C	-299	-256	4.83×10^{-7}	2.73×10^{-6}
D	-282	-201	3.28×10^{-7}	1.86×10^{-6}
E	-273	-163	1.55×10^{-7}	8.40×10^{-7}
F	-293	-158	1.92×10^{-7}	9.36×10^{-7}
G	-295	-166	1.91×10^{-7}	8.82×10^{-7}

E_{corr}：Corrosion potential
E_{pp}：Pitting potential
I_{corr}：Corrosion current density
I_{pp}：Breakdown pitting current density

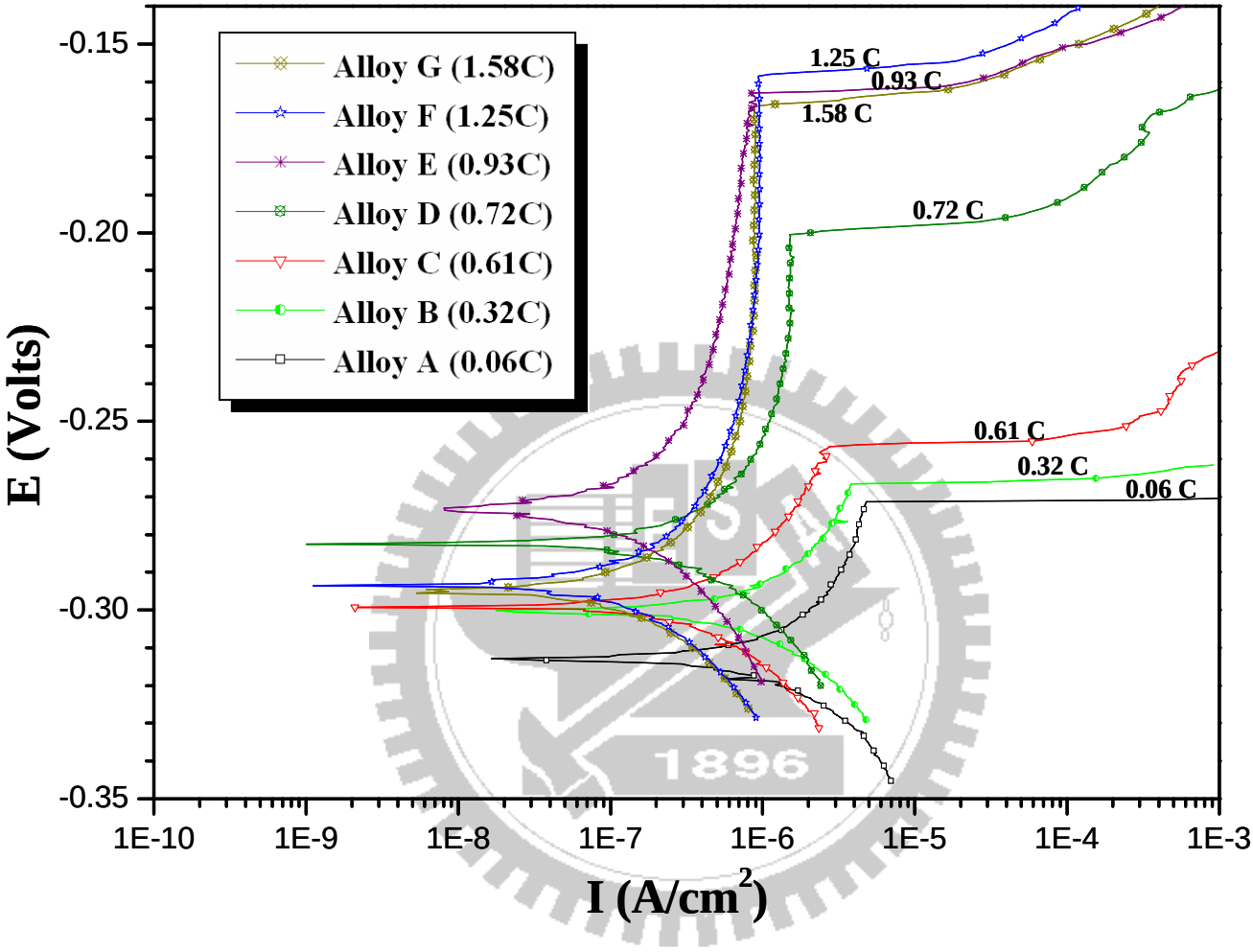

Figure 1. The potentiodynamic polarization curves for the present alloys with various carbon contents in 3.5% NaCl solution.

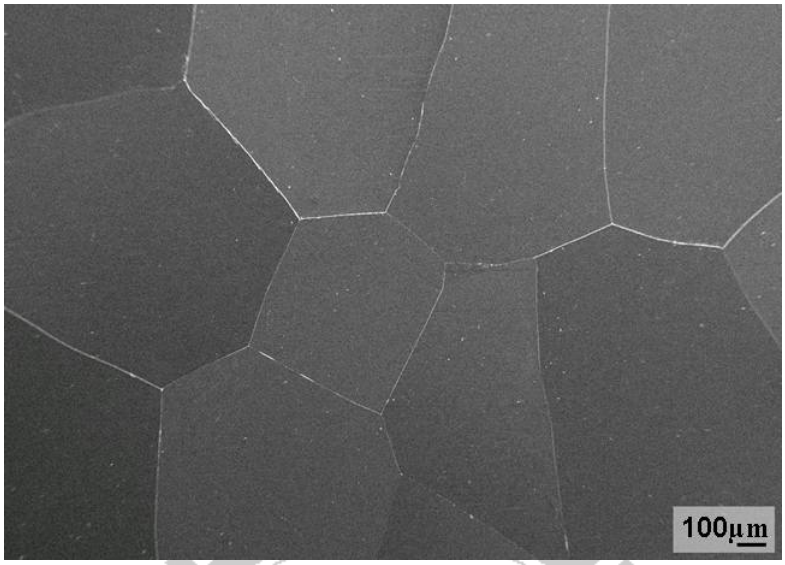

Figure 2(a)

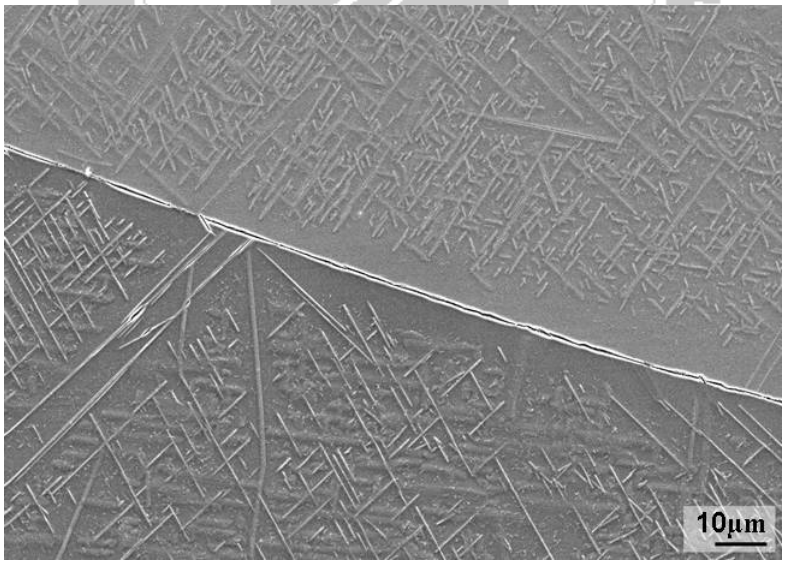

Figure 2(b)

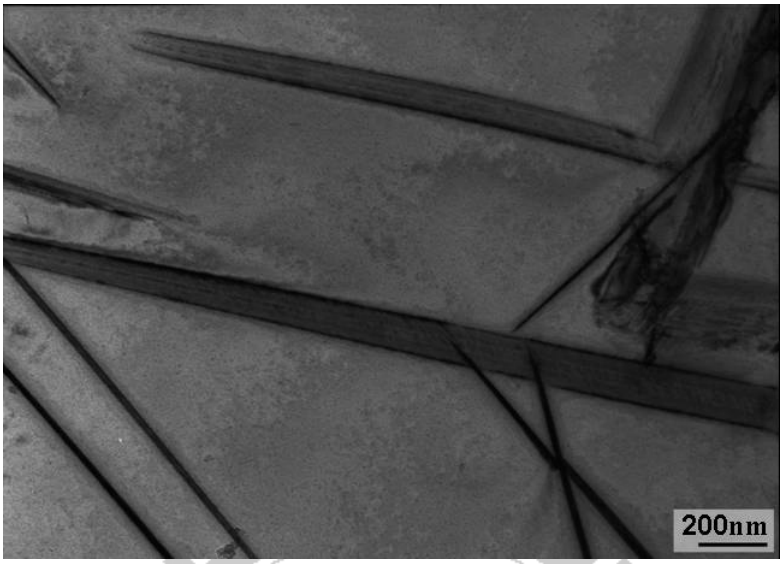

Figure 2(c)

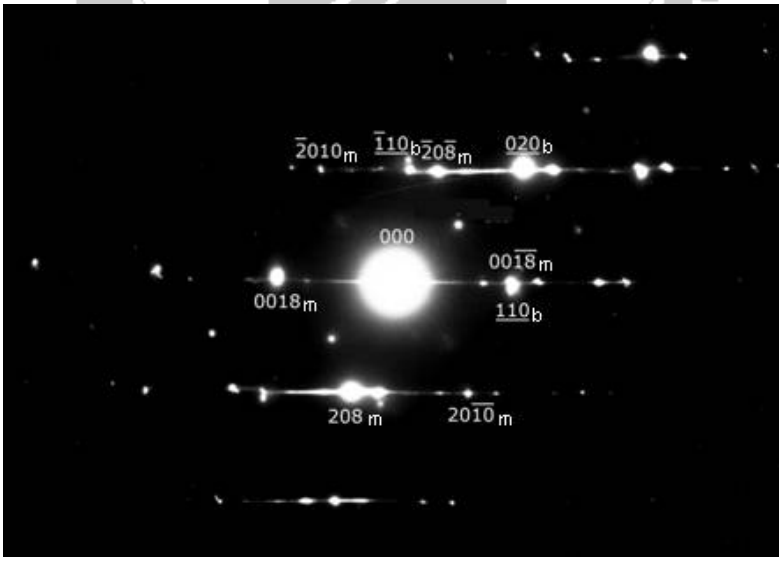

Figure 2(d)

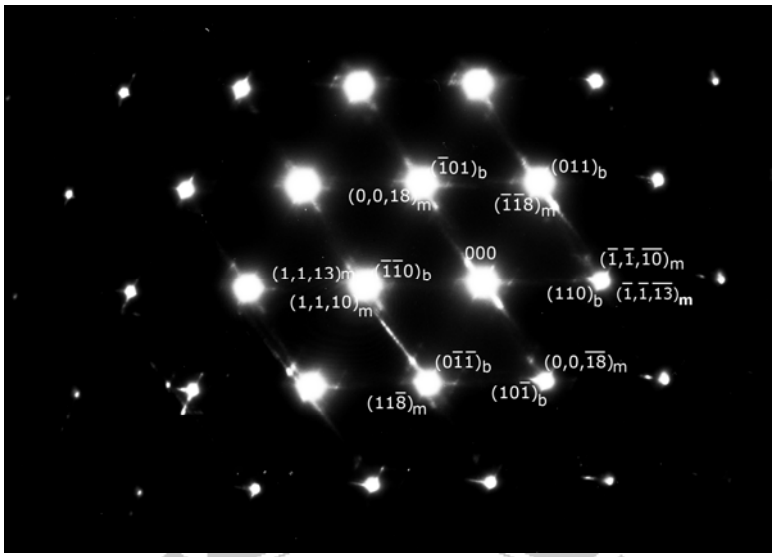

Figure 2(e)

Figure 2. Electron micrographs of the as-quenched alloy A. (a)-(b) low and high magnification SEM micrographs, respectively. (c) TEM bright-field micrograph, (d)-(e) two selected-area diffraction patterns taken from a mixed region covering the needle-like precipitate and the ferrite matrix. The zone axes of the 18R martensite are [010] and $[1\bar{1}0]$, respectively. (m=18Rmartensite, b=ferrite phase)

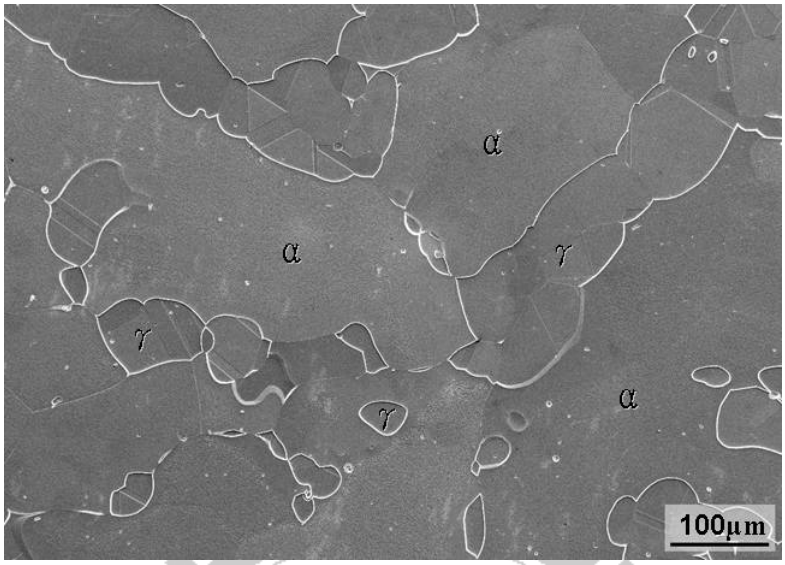

Figure 3(a)

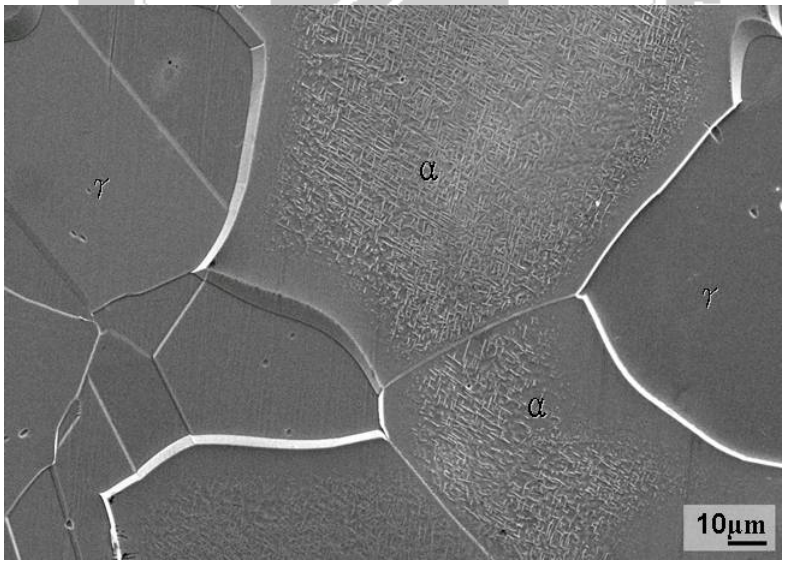

Figure 3(b)

Figure 3. Electron micrographs of the as-quenched alloy B. (a)-(b) low and high magnification SEM micrographs, respectively.

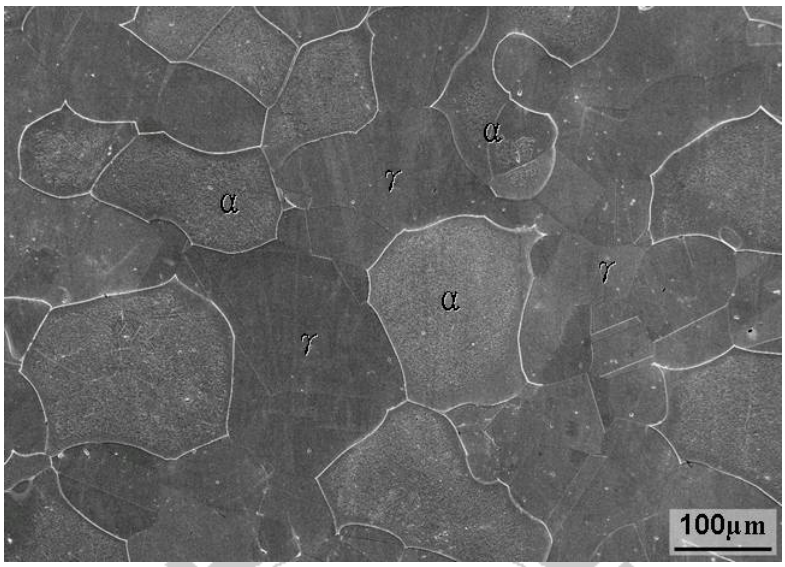

Figure 4(a)

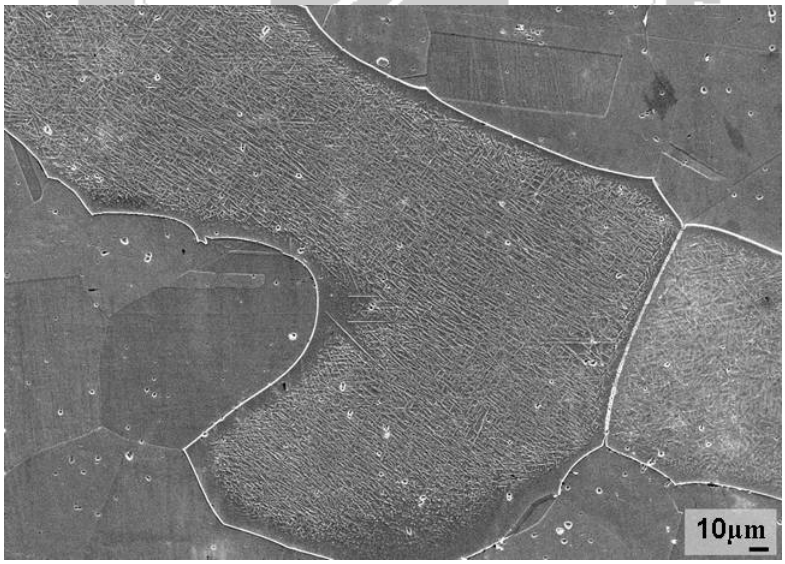

Figure 4(b)

Figure 4. Electron micrographs of the as-quenched alloy C. (a)-(b) low and high magnification SEM micrographs, respectively.

Figure 5

Figure 5. SEM micrograph of the as-quenched alloy D.

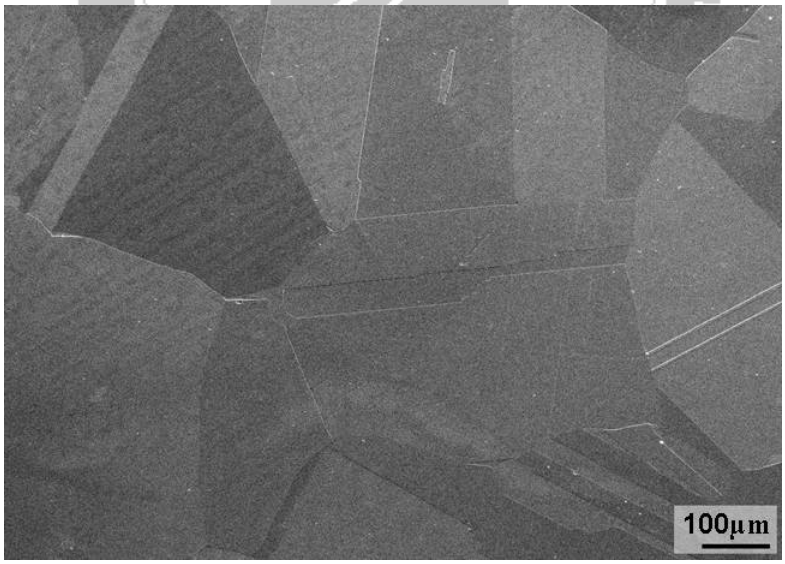

Figure 6

Figure 6. SEM micrograph of the as-quenched alloy E.

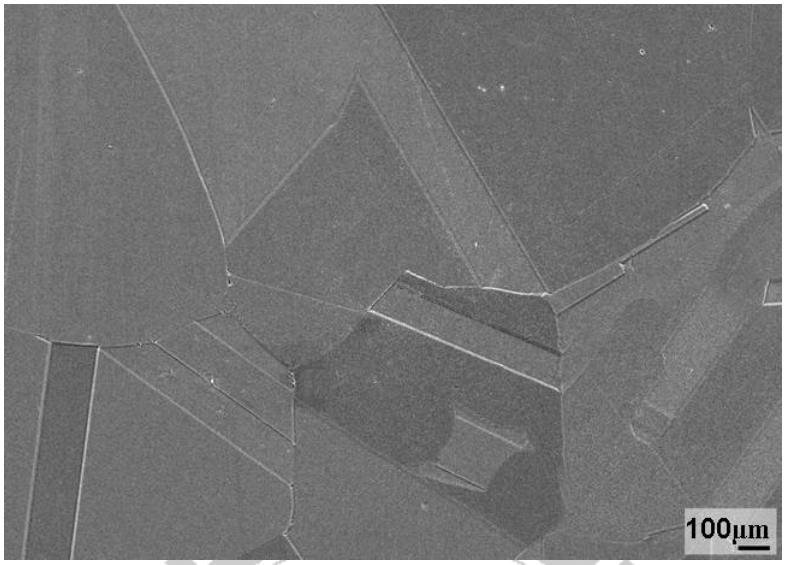

Figure 7(a)

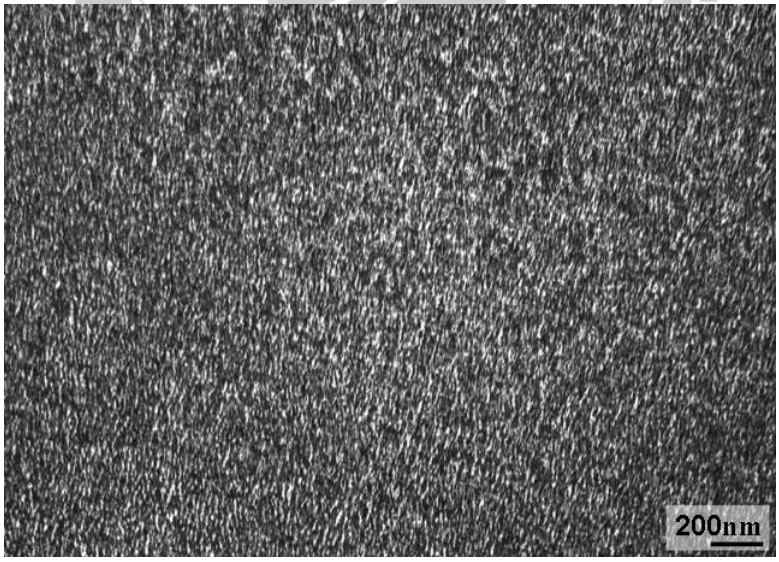

Figure 7(b)

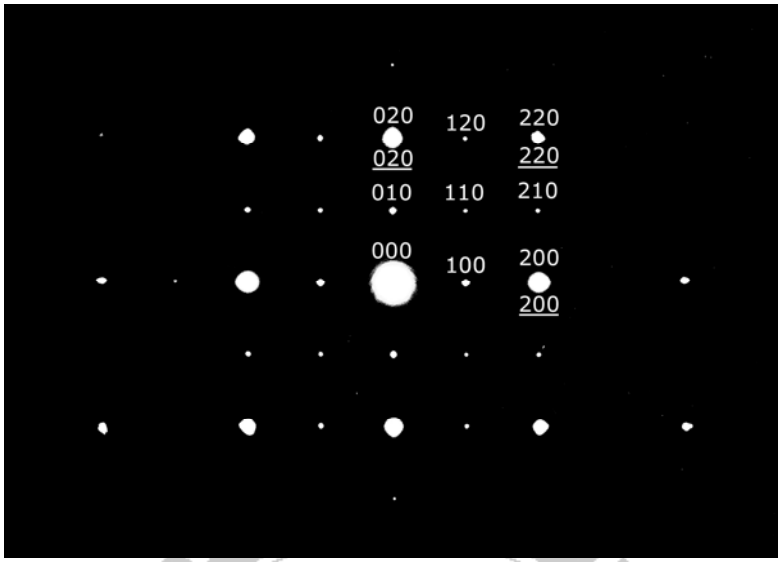

Fig. 7(c)

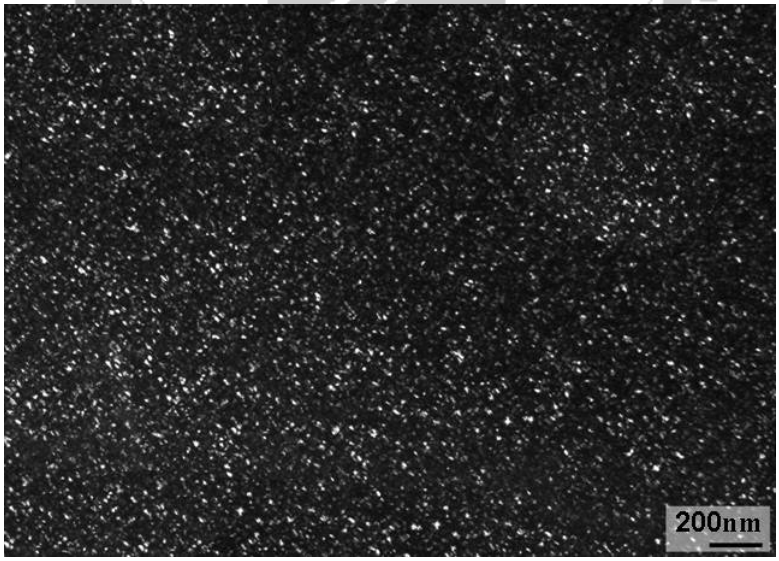

Fig. 7(d)

Figure 7. Electron micrographs of the as-quenched alloy F. (a) SEM micrograph, (b) TEM bright-field micrograph, (c) a selected-area diffraction pattern taken from a mixed region covering the austenite matrix and fine precipitates. The foil normal is [001] (hkl = austenite matrix; hkl = κ'-carbides). (d) 010 κ'-carbide dark-field micrograph.

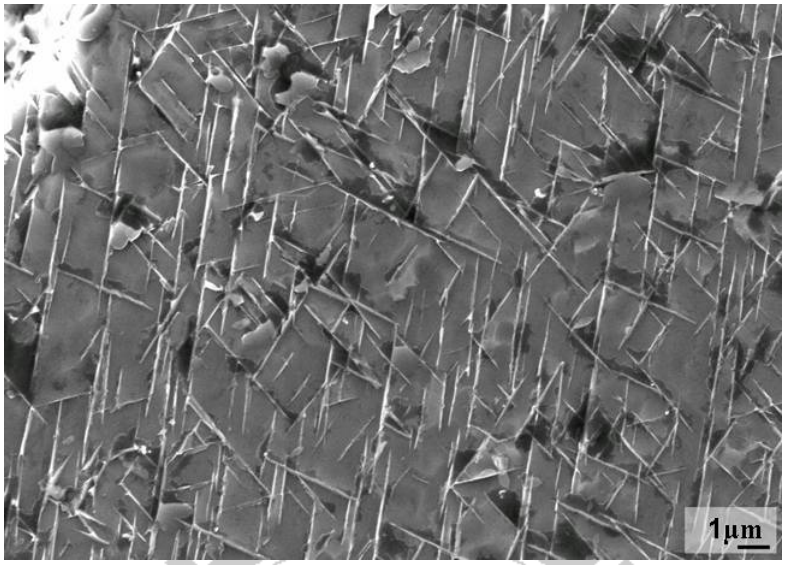

Figure 8(a)

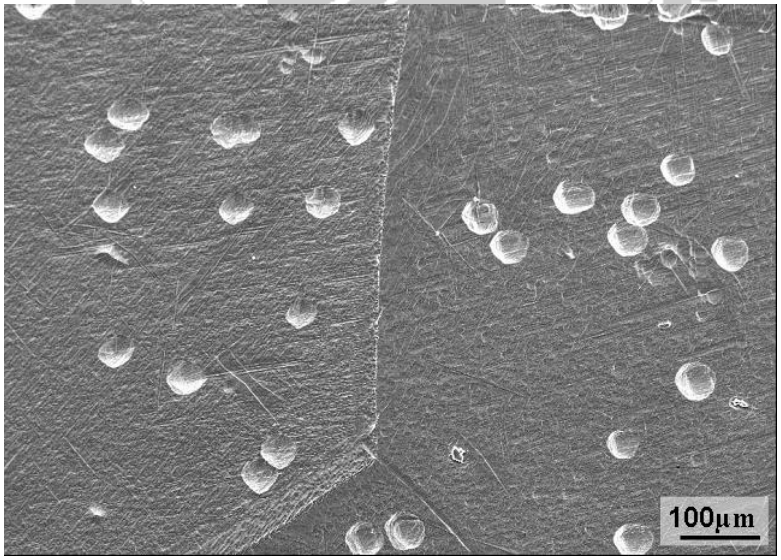

Figure 8(b)

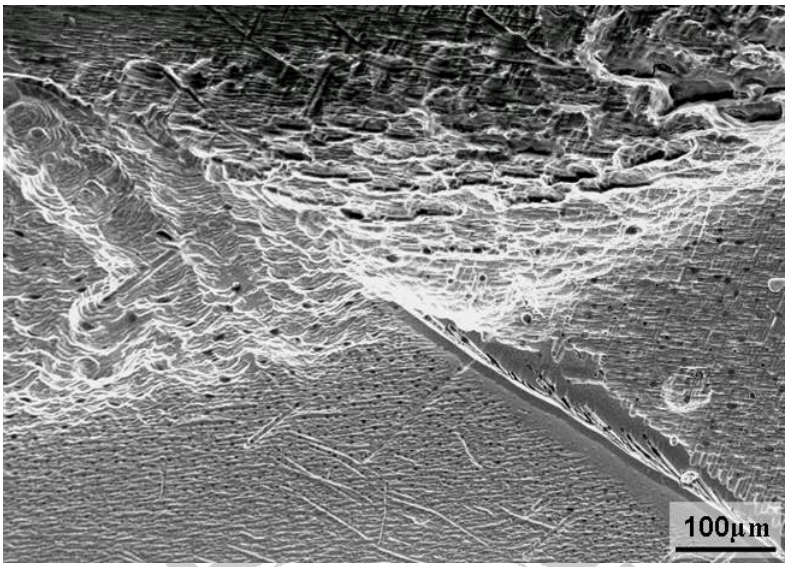

Figure 8(c)

Figure 8. SEM micrograph of the as-quenched alloy A immersed in 6 wt.% $FeCl_3$ solution for (a) 5, (b) 20 minutes and (c) held at pitting potential in 3.5 wt.% NaCl solution for 10 minutes.

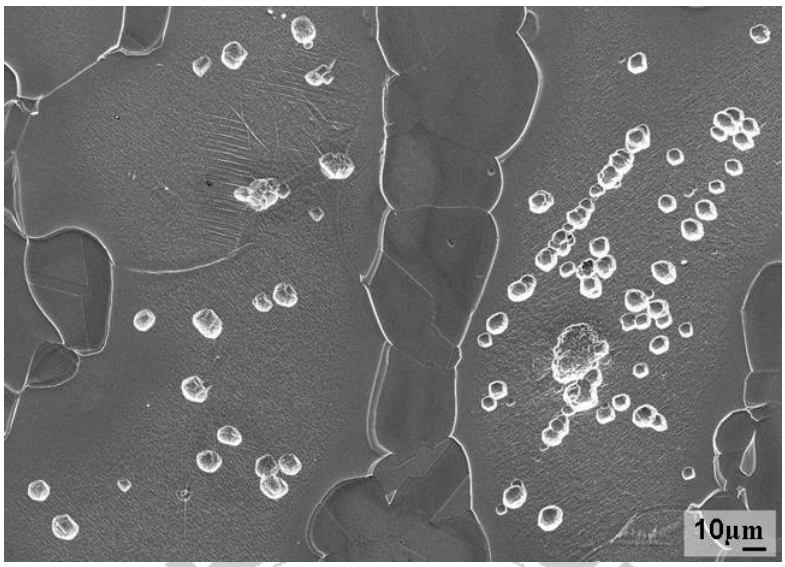

Figure 9(a)

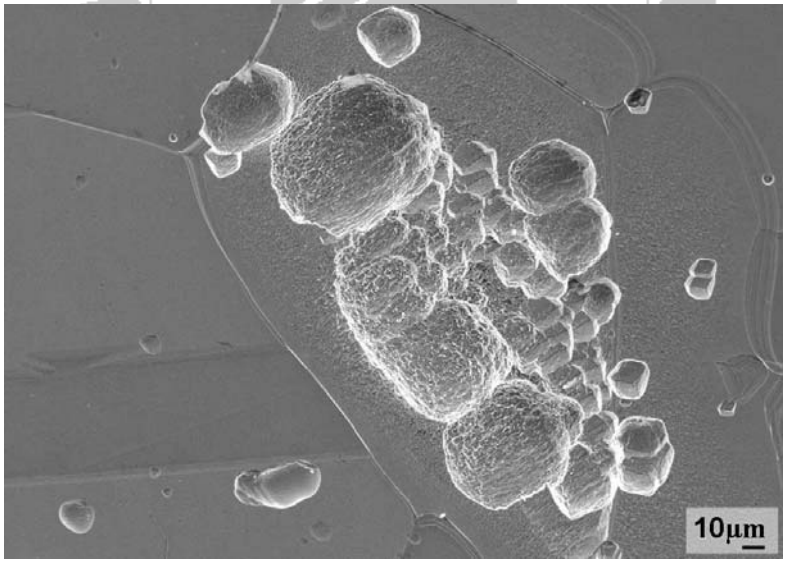

Figure 9(b)

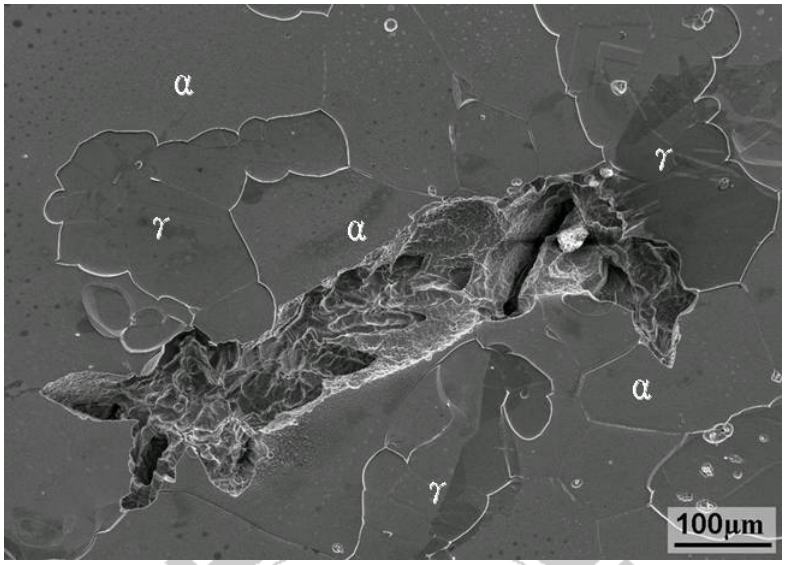

Figure 9(c)

Figure 9. SEM micrograph of the as-quenched alloy B immersed in 6 wt.% $FeCl_3$ solution for (a) 35, (b) 70 minutes and (c) held at pitting potential in 3.5 wt.% NaCl solution for 15 minutes.

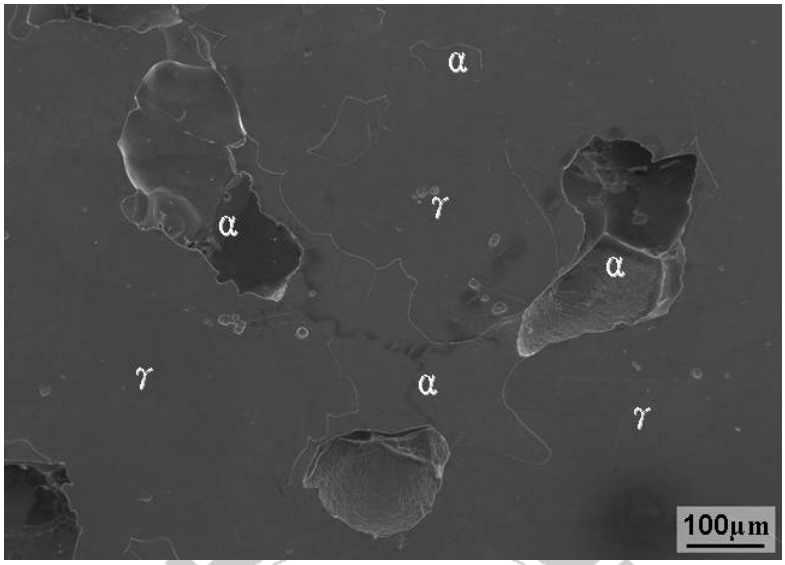

Figure 10

Figure 10. SEM micrograph of the as-quenched alloy C held at pitting potential in 3.5wt.% NaCl solution for 15 minutes.

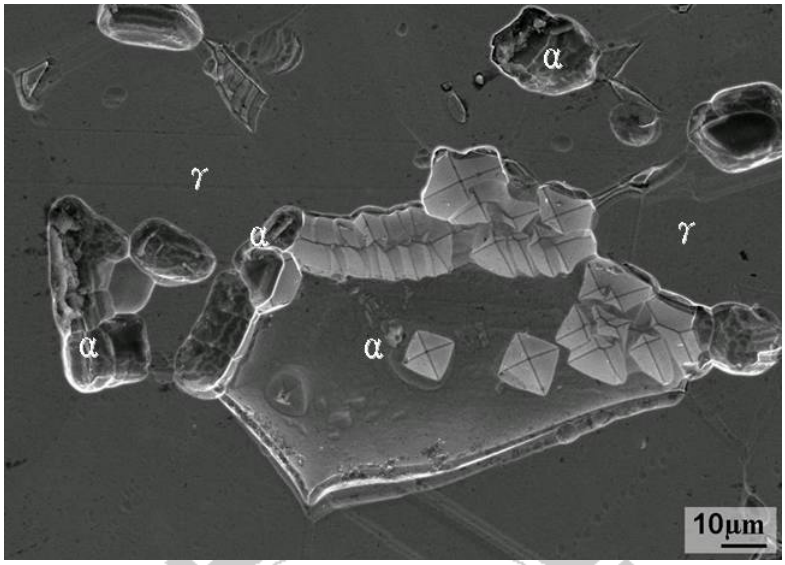

Figure 11(a)

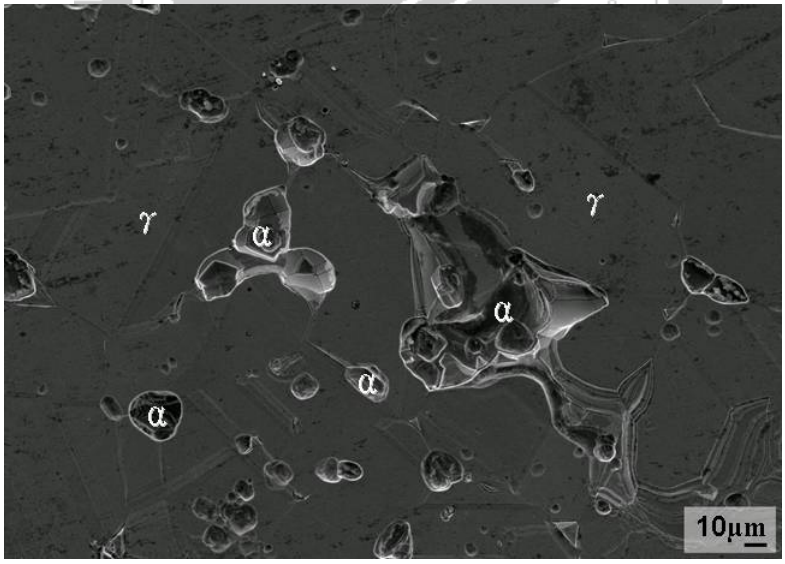

Figure 11(b)

Figure 11. SEM micrograph of the as-quenched alloy D (a) immersed in 6 wt.% $FeCl_3$ solution for 60 minutes, (b) held at pitting potential in 3.5 wt.% NaCl solution for 20 minutes.

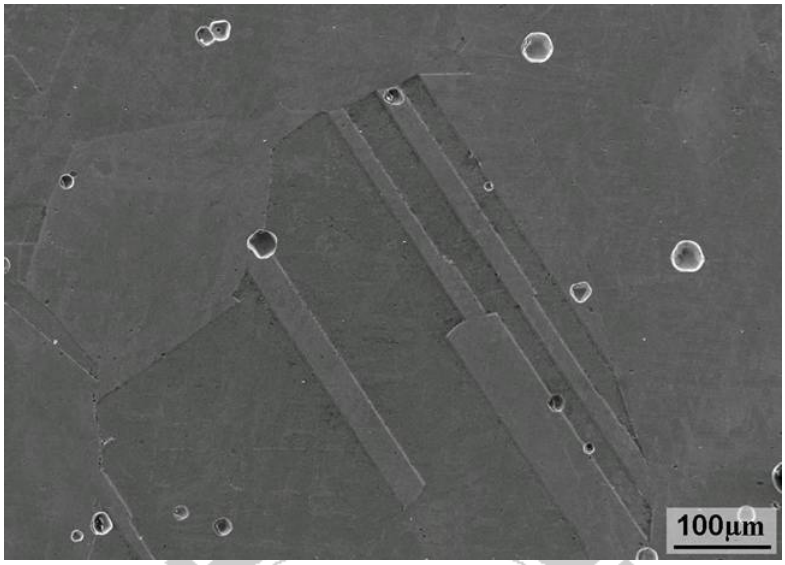

Figure 12(a)

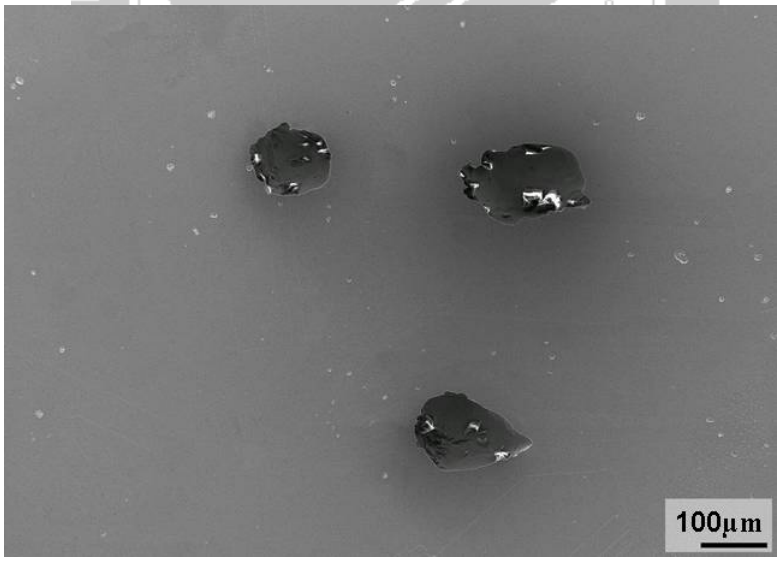

Figure 12(b)

Figure 12. SEM micrograph of the as-quenched alloy E (a) immersed in 6 wt.% $FeCl_3$ solution for 120 minutes, (b) held at pitting potential in 3.5 wt.% NaCl solution for 45 minutes.

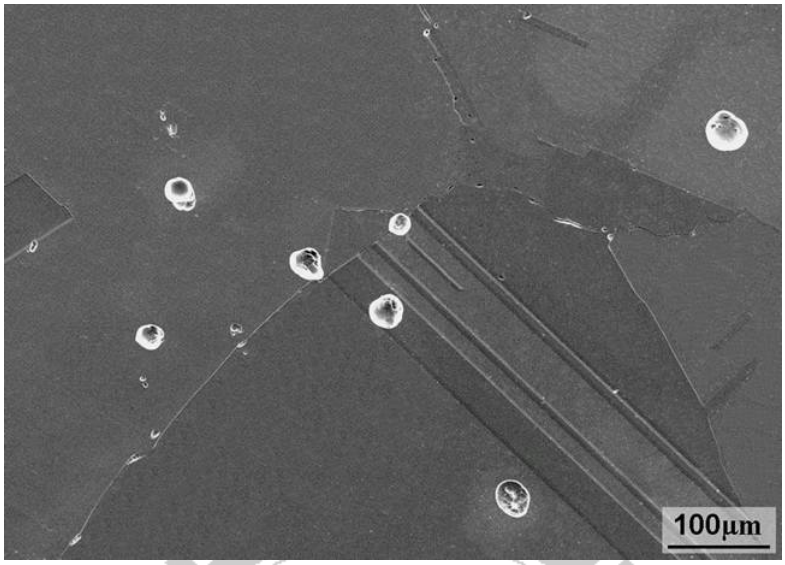

Figure 13(a)

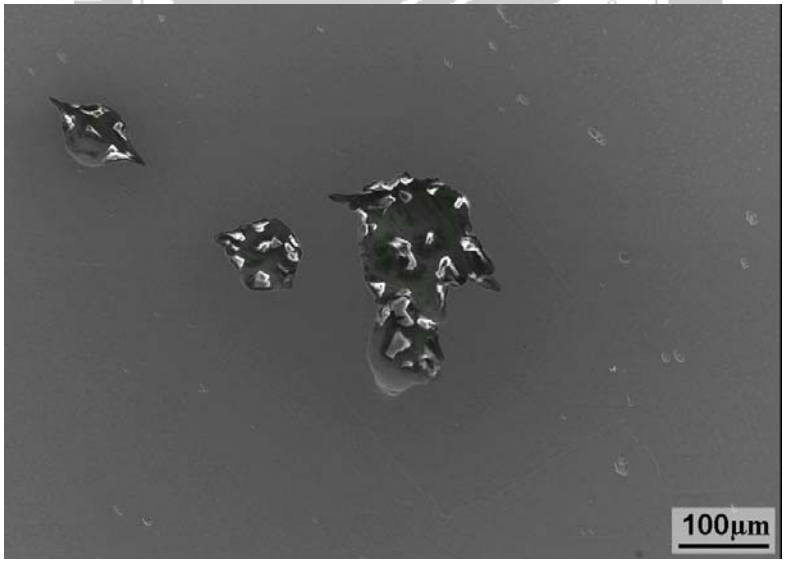

Figure 13(b)

Figure 13. SEM micrograph of the as-quenched alloy F (a) immersed in 6 wt.% $FeCl_3$ solution for 120 minutes, (b) held at pitting potential in 3.5 wt.% NaCl solution for 45 minutes.

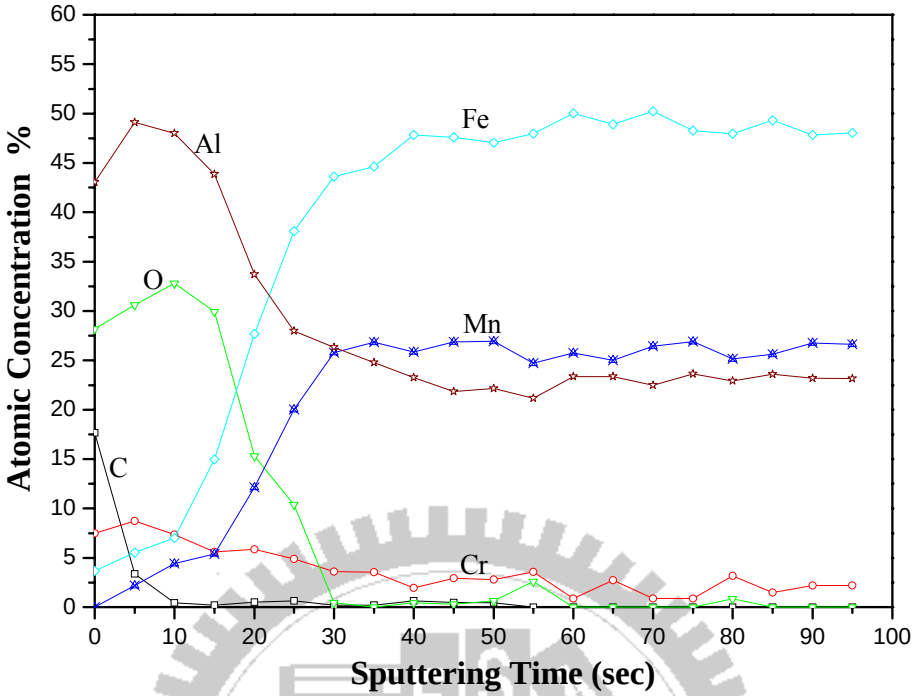

Figure 14(a)

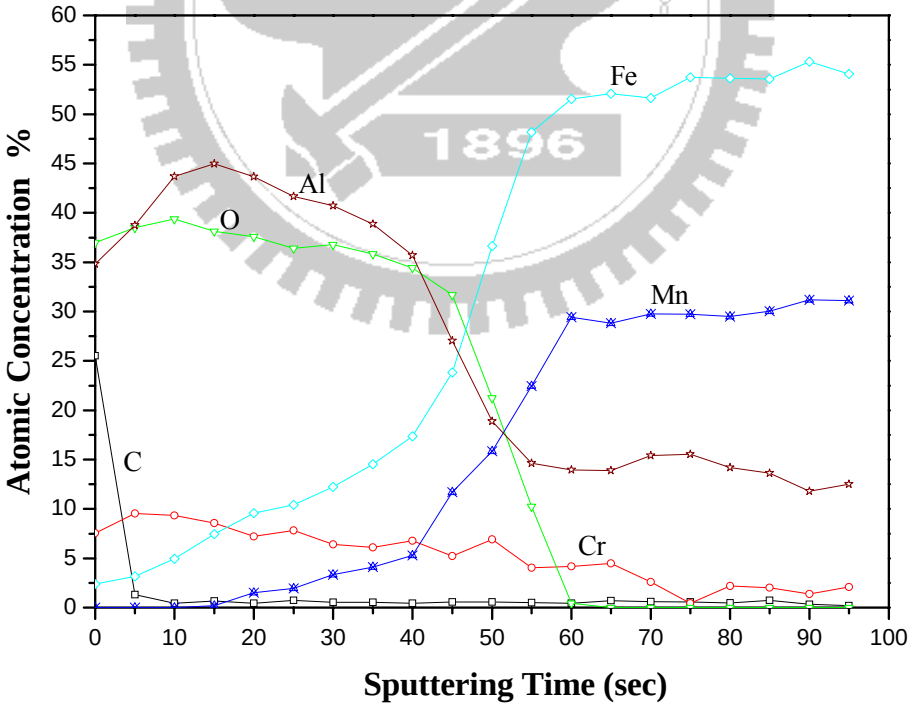

Figure 14(b)

Figure 14. AES concentration depth profiles taken from (a) the austenite phase and (b) the ferrite phase, in the as-quenched alloy D after held at a passive potential for 20 minutes in 3.5 wt.% NaCl solution.